Turkish Journal of Electrical Engineering & Computer Sciences

http://journals.tubitak.gov.tr/elektrik/

Research Article

Turk J Elec Eng & Comp Sci
(2022) 30: 1677 – 1694

doi:10.3906/elk-1300-0632.3898

Comparative study of a bidirectional multi-phase multiinput converter for electric vehicles

Furkan AKAR*, **Murat KALE**, **Sebahattin YALÇIN**, **Gözde TAŞ**
Electrical and Electronics Engineering, Engineering Faculty, Duzce University, Duzce, TURKEY

Received: 26.05.2021 • **Accepted/Published Online:** 20.12.2021 • **Final Version:** 22.07.2022

Abstract: Multiinput converters allow to create hybrid energy systems in electric vehicles with a reduced part count. In addition, interleaved structures help to build efficient converters with several possible benefits, such as low current ripple and high power density. This paper proposes utilizing a multiphase multiinput converter (MPMIC), which concentrates the aforementioned advantages and presents a comprehensive comparison with its single-phase version, called single-phase multiinput converter (SPMIC). After analysing their steady-state characteristics, SPMIC and MPMIC are designed considering same conditions. Then, two laboratory prototypes rated at 2.5kW output power are implemented to validate the analysis. Finally, these prototypes are compared in terms of voltage-gain, input current ripple, efficiency, complexity, cost, and power density. The results show that MPMIC surpasses SPMIC in efficiency and in input current ripple at the expense of increments in the complexity and cost. Besides, MPMIC results in comparatively high voltage gain in low power region thanks to the discontinuous current mode operation. On the other hand, it is explored that SPMIC can reach higher power density in the event of effective cooling.

Key words: Electric vehicle, hybrid energy system, interleaved converter, multiinput converter, multiphase converter

1. Introduction

Hybrid power systems (HPSs) appear to be very promising in satisfying high energy and high power requirements of electric vehicles (EVs) [1, 2]. Controlling the HPSs in full measure is only possible through proper power electronics converters. Utilizing several single-input converters can be considered as a powerful candidate method for building HPSs in EVs. Many works employing this method discuss the utilization of multiphase converters (MPCs) instead of single-phase converters (SPCs) as in [3–5]. In MPCs, the power conversion is realized through parallel legs, which ideally share the power equally. By this way, MPCs allows to improve the converting efficiency by decreasing current stresses and switching losses in spite of increased complexity [6, 7]. Furthermore, it is addressed that filter requirements, inductor sizes, electromagnetic interference problems and hot spots on the printed circuit boards (PCBs) can be reduced thanks to MPCs [8, 9]. According to [10], utilizing multiphases can also help to create cost-effective converters, since they allow choosing circuit elements with low current ratings. Therefore, researchers have proposed several structures in the literature so as to take the advantages MPCs in HPSs for EVs. For instance, the converter presented in [11] is actually composed of an interleaved boost converter and two interleaved buck-boost converter having two-phases; therefore, it has high component count. Furthermore, the converter examined in [12] is basically formed by multiple interleaved boost converter sharing a common output capacitor. A multiphase unidirectional converter, which is actually a

*Correspondence: furkanakar@duzce.edu.tr

three-phase single input boost converter, is studied for FC hybrid electrics in [13]; the conducted experiments and analysis in this work clearly reveal that filter elements, input current ripples, and losses are reduced owing to the interleaving technique. The works in [14] and [15] focus on the applications of different controller methods for four-phase interleaved DC-DC boost converter for hybrid electric vehicles and show the effectiveness of that MPC in high-power applications. The paper in [16] evaluates a two-phase interleaved boost converter for high power electric vehicles applications; although this work validates the analysis through experiments, it compares the studied converter and conventional boost converter only in terms of power density.

Unfortunately, creating HPSs in EVs through separate single-input converters may suffer from complexity, high cost, and control difficulties [17]. Alternatively, another method suggests employing multi-input converters (MICs) in order to create cost-effective, reliable, and easily controllable HPSs as reported in [18] and [19]. There have been some efforts to combine the advantages of MPCs and MICs. For example, a simulation based study is given in [20] for satellite subsystems; a unidirectional multi-input multi-output interleaved boost converter, allowing up to two input sources and operating only in boost mode, is proposed in this work. Authors in [21] study on an unidirectional converter, which is formed by replacing input sources in an interleaved boost converter with H-bridge cells; therefore, the number of inputs in this converter is arbitrary. Unfortunately, the converter in [21] operates only in boost mode without power flow capability between sources. In [22], authors propose a structure consisting of two parallel interleaved boost converters connected to a switched capacitor network; although this converter have several advantages, such as, unlimited input sources, bidirectional power flow capability, high voltage gain, it does not allow buck operation and power flow between sources. A multiphase MIC, formed by connecting two boost converters indirectly in series to attain high voltage gain, is proposed and tested experimentally in [23]; this converter operates as an MPC in the individual supplying power mode, however, operates as an SPC the simultaneous supplying power mode, since each input is connected to a single inductor. In addition, the input switches in [23] designating the operation modes may result in efficiency drop and control difficulties.

Table 1 summarizes the literature review regarding the MPCs creating HPSs in EVs. According to this table, none of the papers examined here success to fulfil all of the requirements of an EV application. Moreover, although some of them include experimental results to validate the theoretical analyses, they exert no effort to benchmark the offered structures and their conventional counterparts experimentally. For making up this deficiency, this paper aims to evaluate a MIC suitable for EV applications considering the single-phase and multiphase cases based on the developed prototypes.

The studied bidirectional MIC for the single-phase and multiphase cases are shown in Figure 1 when it has two inputs. According to papers in [24–26], this converter in both cases offers flexibility in terms of number of input ports. Moreover, it has ability to operate in both buck and boost modes in both directions. Since the converter is bidirectional, there are two main operation modes: discharging mode and charging mode. Input energies flow to the output in the discharging mode and the energy from the output charges the input sources in the charging mode. Although the converter makes the power flow between sources possible, it does not considered in this paper. The presented comparison between single-phase and multiphase structures in this work takes account of several aspects, i.e., voltage-gain, input current ripple, efficiency, complexity, cost, and power density.

Table 1. Comparison of the proposed MPMIC with similar structures.

	Multi-input	Buck capability	Power flow between sources	Bidirectional operation	Experiment
[11]	No	No	Yes	Yes	No
[12]	No	No	No	No	No
[13, 16]	No	No	No	No	Yes
[14]	No	No	Yes	Yes	Yes
[20]	Yes	No	Yes	No	No
[21]	Yes	No	No	No	No
[22]	Yes	No	No	Yes	No
[23]	Yes	No	No	No	Yes
Proposed	Yes	Yes	Yes	Yes	Yes

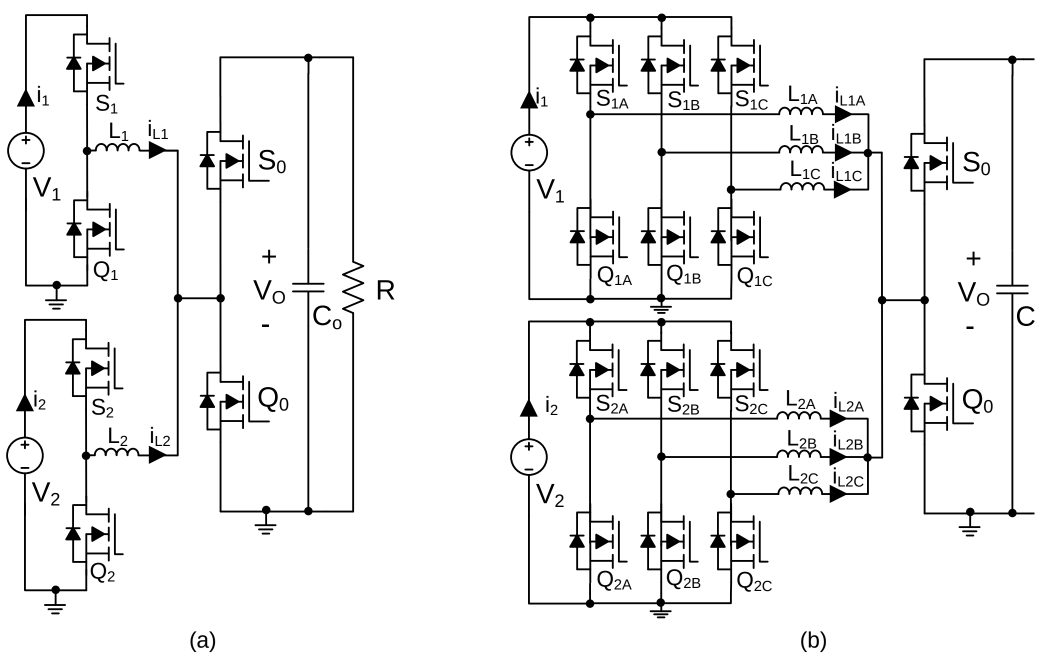

Figure 1. The bidirectional (a) single-phase, (b) multiphase multiinput converters.

2. Single-phase multi-input converter

The single-phase multi-input converter (SPMIC) is shown in Figure 1(a). In the discharging mode, high-side input switches (S_1 and S_2) and low-side output switch (Q_0) are controlled by pulse-width-modulation (PWM). In the charging mode, low-side input switches (Q_1 and Q_2) and high-side output switch (S_0) are controlled by PWM. The analysis given in this paper is carried out for the steady-state operation by assuming ideal elements and constant output voltage during one switching period. The duty cycles of input switches are denoted by d_1 and d_2 in both operation modes for the first and second inputs, respectively; while, the duty cycles of output switches are denoted by d_0. In the analysis, it is assumed that $V_1 < V_o < V_2$ in order to consider buck and boost modes. Therefore, $d_2 < d_0' < d_1$ must be met in the discharging mode, while $d_2' < d_0 < d_1'$ must be met in the charging mode. Please note that $d_0' = 1 - d_0$, $d_1' = 1 - d_1$, and $d_2' = 1 - d_2$. Furthermore, the inductors are assumed to have equal inductance at L for ease of reading.

2.1. Discharging mode

Figure 2 shows typical waveforms for SPMIC operating in the discharging mode for one switching period (T) considering continuous conduction mode (CCM) and discontinuous conduction mode (DCM). Please note that readers are referred to [27] for the details of CCM analysis and equivalent circuits encountered in this mode.

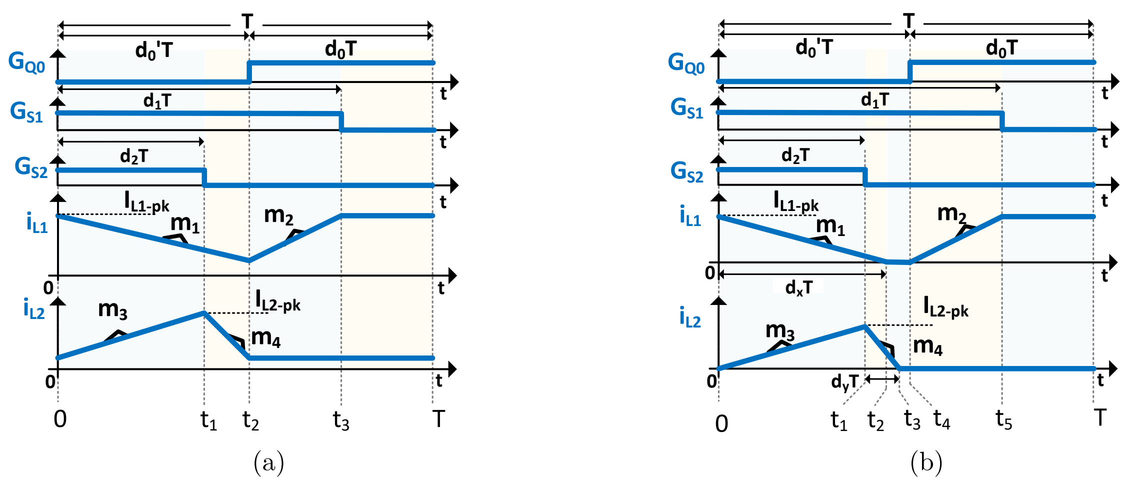

Figure 2. Discharging mode waveforms for SPMIC in a) CCM, b) DCM.

2.1.1. CCM operation

According to [27], the inductor current slopes indicated in Figure 2a can be given as follows:

$$
\begin{aligned}
m_1 &= (V_1 - V_o)/L, \\
m_2 &= V_1/L, \\
m_3 &= (V_2 - V_o)/L, \\
m_4 &= -V_o/L.
\end{aligned} \tag{1}
$$

Moreover, the voltage gain for SPMIC operating in the discharging mode for CCM can be expressed as in (2) where subscript $i = 1, 2$.

$$V_o/V_i = d_i/d_0' \tag{2}$$

The current relationship can be given as in (3) where I_1 and I_2 are average inductor currents, while R is the output load.

$$(I_1 + I_2)d_0' = V_o/R \tag{3}$$

Based on (2) and inductor current slopes, inductor current ripple for two cases can be calculated as in

$$\Delta I_{Li} = \begin{cases} V_i(d_i - d_0')/(fL), & \text{if } d_i > d_0' \\ V_i d_i(d_0' - d_i)/(d_0' fL), & \text{if } d_i < d_0'. \end{cases} \tag{4}$$

Then, inductor peak currents can be computed as in

$$I_{Li-pk} = I_i + \begin{cases} \Delta I_{Li} d_i/2, & \text{if } d_i > d_0' \\ \Delta I_{Li}(2 - d_0')/2, & \text{if } d_i < d_0'. \end{cases} \tag{5}$$

2.1.2. DCM operation

There are six distinct subintervals when the SPMIC operates in discharging mode in DCM as shown in Figure 2b. Here $d_x < d_0'$ while $d_y < d_0' - d_2$.

$Subinterval - 1$ $[0 < t < t_1]$: This subinterval is equivalent to the first subinterval in CCM except that the current of i_{L2} starts from zero. The slopes of i_{L1} and i_{L2} are equal to m_1 and m_3, respectively.

$Subinterval - 2$ $[t_1 < t < t_2]$: This period starts when S_2 becomes ON and finishes when i_{L1} drops the zero. The slope of i_{L1} is still m_1 while the slope of i_{L2} becomes m_4.

$Subinterval - 3$ $[t_2 < t < t_3]$: In this period, i_{L1} is zero; therefore, its slope is zero. i_{L2} continues to decrease with the slope of m_4 and finally drops to zero at the end of this period.

$Subinterval - 4$ $[t_3 < t < t_4]$: In this period, both inductor currents are zero; thus, both slopes are zero.

$Subinterval - 5$ $[t_4 < t < t_5]$: This subinterval is initiated by turning Q_0 ON at $t = t_4$. L_1 is charged by the first input; therefore, its current slope becomes m_2, while i_{L2} is still zero, since S_2 is still opened.

$Subinterval - 6$ $[t_5 < t < T]$: In the final subinterval, S_1 becomes OFF. The slope of i_{L1} becomes zero; thus, it stays at its peak value.

By using volt-second-balance (VSB) on L_1 and L_2, the output voltage for SPMIC operating in the discharging mode for DCM can be expressed as follows:

$$V_o = V_1(d_x + d_1 - d_0')/d_0' = V_2 d_2/(d_2 + d_y). \tag{6}$$

By using ASB on C_o, the following equation can be obtained:

$$I_1 d_x + I_2(d_2 + d_y) = V_o/R. \tag{7}$$

Inductor peak currents (=current ripples) in DCM can be computed as follows:

$$I_{Li-pk} = \begin{cases} V_i(d_i - d_0')/(fL), & \text{if } d_i > d_0' \\ (V_i - V_o)d_i/(fL), & \text{if } d_i < d_0'. \end{cases} \tag{8}$$

Then, the average inductor currents can be calculated as in (9).

$$I_i = \begin{cases} (1/2)I_{Li-pk} d_x, & \text{if } d_i > d_0' \\ (1/2)I_{Li-pk}(d_i + d_y), & \text{if } d_i < d_0'. \end{cases} \tag{9}$$

By assuming single source operation, the voltage gain of SPMIC operating in the discharging mode in DCM can be calculated based on (6)-(9) as in

$$V_o/V_i = \begin{cases} \left(1+\sqrt{1+4(d_i-d_0')^2/K}\right)/2, & d_i > d_0' \\ 2/\left(1+\sqrt{1+4K/d_i^2}\right), & d_i < d_0' \end{cases} \tag{10}$$

where K is dimensionless parameter which is expressed as in

$$K = 2L/(RT). \tag{11}$$

Now, SPMIC can be analyzed in boundary conduction mode (BCM).

2.1.3. BCM Operation

At the boundary between CCM and DCM, the voltage gains become equal. Therefore, critical value of the K for SPMIC in the discharging mode can be calculated based on (2) and (10) as in

$$K_{crit} = \begin{cases} d_0'^2(d_i - d_0')/d_i, & \text{if } d_i > d_0' \\ d_0'(d_0' - d_i), & \text{if } d_i < d_0'. \end{cases} \tag{12}$$

In Figure 3, discharging mode characteristic curves of SPMIC for CCM, DCM, and BCM regions are given. According to this figure, the converter operates in CCM if K is higher than K_{crit}, otherwise operates in DCM. Higher d_0' results in higher K_{crit} by addressing decreased current stresses. Moreover, d_i is higher than d_0' in boost mode, while lower than d_0' in buck mode in both CCM and DCM. Furthermore, the voltage gain increases in DCM as in classical buck and boost converters.

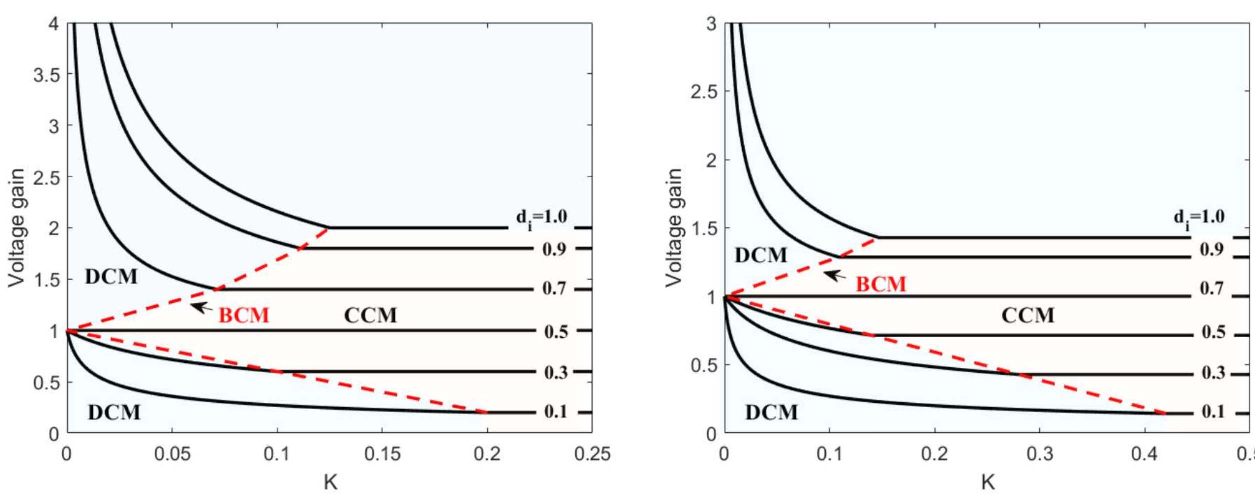

(a) (b)

Figure 3. Discharging mode characteristic curves of SPMIC under CCM, DCM, and BCM regions for a) $d_0' = 0.5$, and (b) $d_0' = 0.7$.

2.2. Charging mode

In this mode, the inductor currents become negative by indicating that the power flows from the output to the inputs. Actually, when the subscript i is changed to o and o is changed to i, the related equations for the charging mode can be obtained based on the discharging mode equations. Therefore, characteristic curves for the charging mode is same with the one of the discharging mode demonstrated in Figure 3 when changing subscripts as mentioned.

3. Multiphase multiinput converter

The multiphase multiinput converter (MPMIC) is depicted in Figure 1(b) for 3-phase case. Here, switches and inductors forming phases are classified via A, B, and C subscripts. In the discharging mode, input switches (S_{1A}, S_{1B}, S_{1C}, S_{2A}, S_{2B}, S_{2C}) and low-side output switch (Q_0) are controlled by PWM. Moreover, in the charging mode, low-side input switches (Q_{1A}, Q_{1B}, Q_{1C}, Q_{2A}, Q_{2B}, Q_{2C}) and high-side output switch (S_0) are controlled by PWM. For achieving same effective switching frequency, the output switches switching frequency are 3 times of the input switches switching frequency. There are also $120°$ between gate signals of input switches for interleaving operation.

In the steady state analysis for MPMIC, it is also assumed that circuit elements are ideal, and output voltage is constant during one switching period. Furthermore, the duty cycles of the first input switches are same at d_1, while the duty cycles of the second input switches are same at d_2 in both operation modes by assuming perfect current sharing between phases. The duty cycles of output switches are again denoted by d_0. Since each input has identical steady state waveforms with $120°$ phase shift, $A-phase$ is considered in the analysis. Here, the voltage levels are again as $V_1 < V_o < V_2$. Therefore, $d_2 < d_0' < d_1$ must be met in the discharging mode, while $d_2' < d_0 < d_1'$ must be met in the charging mode for CCM operation. However, it is not possible to come up with simple inequalities for DCM operation because of the load dependence. Similarly, all inductors in MPMIC have equal inductance at L in the analysis.

3.1. Discharging mode

Figure 4 shows typical waveforms for MPMIC when it operates in the discharging mode for 3 switching periods for CCM and DCM operations. For the equivalent circuits encountered in the subintervals analysed below, readers are referred to [27] again.

3.1.1. CCM operation

According to Figure 4, there are 8 subintervals when the MPMIC operates in discharging mode in CCM.

$Subinterval-1$ $[0 < t < t_1]$ and $Subinterval-3$ $[t_2 < t < t_3]$: In these periods, Q_0 is OFF while S_{1A} and S_{2A} are ON. Therefore, L_{1A} and L_{2A} current slopes are equal to m_1 and m_3, respectively.

$Subinterval-2$ $[t_1 < t < t_2]$: This subinterval starts when Q_0 becomes ON. So, L_{1A} and L_{2A} are charged by the input sources with the slopes of m_2 and m_5, respectively, where m_5 is equal to V_2/L.

$Subinterval-4$ $[t_3 < t < t_4]$ and $Subinterval-6$ $[t_5 < t < t_6]$: These subintervals are started by turning S_{2A} OFF at $t = t_3$. Therefore, the slope of i_{L2A} becomes m_4, while the slope of i_{L1A} is still m_1.

$Subinterval-5$ $[t_4 < t < t_5]$: At $t = t_4$, Q_0 is turned OFF, while S_{1A} is ON and S_{2A} is OFF. Therefore, L_{1A} is being charged by the first input, while the current of L_{2A} remains constant because of freewheeling. The slopes of i_{L1A} and i_{L2A} are equal to m_2 and 0, respectively.

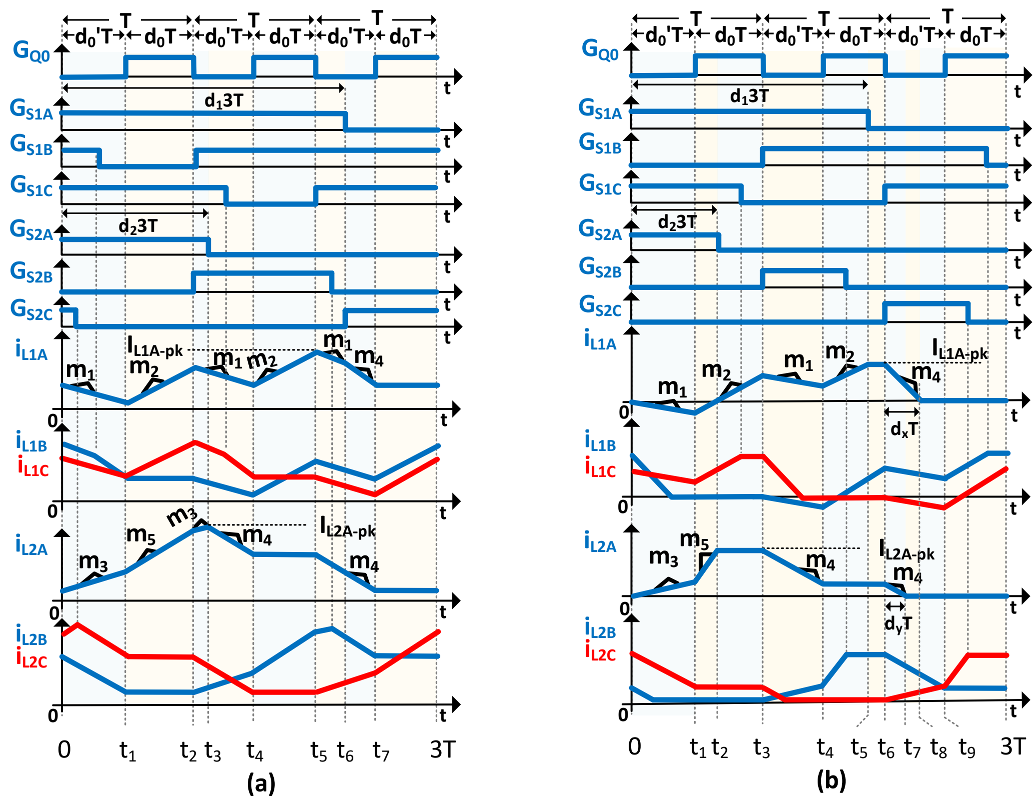

Figure 4. Discharging mode waveforms for the MPMIC in a)CCM, b)DCM.

Subinterval $-$ 7 $[t_6 < t < t_7]$: Turning OFF S_{2A} starts this period. Therefore, the L_{1A} feeds the output like L_{2A}. Both slopes are equal to m_4.

Subinterval $-$ 8 $[t_7 < t < 3T$: In the final subinterval, Q_0 is again closed. Since both input switches are being kept opened, both inductor current slopes are zero; therefore, currents remain constant.

By using VSB on L_{1A} and L_{2A}, it can be explored that the voltage gain for MPMIC in the discharging mode in CCM is same with the one for SPMIC given in (2).

The current ripples in CCM can be computed based on the current slopes which are altered according to the operation mode (buck or boost). Moreover, the forms of the inductor current waveforms, depending upon on the relationship between the duty cycles of input and output switches, need to be considered. For example, according to Figure 4, when $2 < 3d_i < 2 + d_0'$ and the converter is in boost mode, the current ripple can be calculated for considering the slopes given for i_{L1A} between t_1 and t_5. Besides, when $1 < 3d_i < 1 + d_0'$ and the converter is in buck mode, the slopes given for i_{L2A} between 0 and t_3 need to be taken into account. By following this procedure, the current ripples expressions are obtained for all cases, which can be found in Table 2.

In order to correlate the peak inductor current with average inductor current as in (5), areas under the current waveforms given in Figure 4 must be calculated. This work is quite challenging since these waveforms are irregular and depend on the cases studied in Table 2. Therefore, an approximation is proposed in order to

Table 2. Inductor current ripples for MPMIC in the discharging mode

	Buck	Boost
$0 < 3d_1 < d_0'$	$\frac{(V_i - V_o)3d_1}{fL}$	–
$d_0' < 3d_1 < 1$	$\frac{V_i 3d_1 - V_o d_0'}{fL}$	$\frac{V_i(3d_1 - d_0')}{fL}$
$1 < 3d_1 < 1 + d_0'$	$\frac{V_i 3d_1 - V_o(3d_1 - d_0)}{fL}$	$\frac{V_i d_0}{fL}$
$1 + d_0' < 3d_1 < 2$	$\frac{V_i 3d_1 - V_o 2d_0'}{fL}$	$\frac{V_i(3d_1 - d_0') - V_o d_0'}{fL}$
$2 < 3d_1 < 2 + d_0'$	$\frac{V_i 3d_1 - V_o(3d_1 - 2d_0)}{fL}$	$\frac{V_i(2 - d_0') - V_o d_0'}{fL}$
$2 + d_0' < 3d_1 < 1$	–	$\frac{V_i(2 - d_0') - V_o d_0'}{fL}$

calculate the peak inductur current in the discharging mode in CCM for MPMIC as in

$$I_{Li-pk} \approx I_i + \Delta I_{Li}(2 - d_1)/2 \tag{13}$$

where ΔI_{Li} can be calculated through Table 2 for a given case.

3.1.2. DCM operation

According to Figure 4, there are 10 subintervals in 3 switching periods when MPMIC operated in the discharging mode in DCM. Here $d_x < d_0'$ and $d_y < d_0'$.

$Subinterval - 1$ $[0 < t < t_1]$: The first subinterval in DCM is equivalent to the first subinterval in CCM for the discharging mode except that both inductor current are zero at the beginning of the subinterval for DCM. It is interesting to note that i_{L1A} becomes negative here, since Q_0 is OFF, and $V_1 < V_o$ makes the the voltage on L_{1A} negative. Therefore, the body diode of S_{1A} starts to conduct to carry negative i_{L1A}.

$Subinterval - 2$ $[t_1 < t < t_2]$: This subinterval is initiated by closing Q_0 at $t = t_1$. Therefore, L_{1A} and L_{2A} have positive slopes m_2 and m_5, respectively. Therefore, both inductor currents increase.

$Subinterval - 3$ $[t_2 < t < t_3]$ and $Subinterval - 5$ $[t_4 < t < t_5]$: S_{2A} is turned OFF and these periods start. i_{L2A} becomes constant since Q_0 is still ON while the slope of i_{L1A} is still m_2.

$Subinterval - 4$ $[t_3 < t < t_4]$: In this subinterval, Q_0 becomes OFF. Therefore, both inductors start to dishcarge. The slope of i_{L1A} becomes m_1 again, while the slope of i_{L2A} becomes m_4.

$Subinterval - 6$ $[t_5 < t < t_6]$: At $t = t_5$, S_{1A} becomes OFF. Thus, the freewheeling period for L_{2A} also starts. In other words, both inductor currents stay constant during this subinterval.

$Subinterval - 7$ $[t_6 < t < t_7]$: This subinterval is started by opening Q_0 at $t = t_6$ while both input switches are OFF. Therefore, both inductors discharge with the slope of m_4.

$Subinterval - 8$ $[t_7 < t < t_8]$: At the beginning of the previous subinterval, both inductor current started to decrease. This subinterval starts when i_{L2A} becomes zero at $t = t_7$.

$Subinterval - 9$ $[t_8 < t < t_9]$: At $t = t_8$, i_{L1A} also becomes zero, and this period starts.

$Subinterval - 10$ $[t_9 < t < 3T]$: In this period, turning Q_0 ON does not affect inductor currents. Both stay at zero.

By applying VSB principle to inductor waveforms in Figure 4, the output voltage for DCM can be expressed as follows:

$$V_o = (3V_1 d_1)/(2d_0' + d_x) = (3V_2 d_2)/(2d_0' + d_y). \tag{14}$$

By assuming perfect current sharing between phases and applying ASB on C_o, the following equation can be written:

$$I_1(2d_0' + d_x) + I_2(2d_0' + d_y) = V_o/(3R) \tag{15}$$

The peak currents in DCM is equal to the current ripples given in Table 2 for buck operation, while the peak currents for boost operation can be calculated as follows:

$$I_{Li-pk} = \Delta I_{Li} - \frac{(V_o - V_i)d_0'}{fL} \tag{16}$$

In order to calculate the voltage-gain of MPMIC in DCM, the expressions for average inductor currents must be obtained by analysing current waveforms presented in Figure 4. Although, this difficult task can be made easier through some approximations, it is decided to perform a parameter sweep analysis in PSIM environment here for better accuracy.

3.1.3. BCM operation

Another parameter sweep analysis is realized in PSIM to tobtain K_{crit} variations. The results for the parameter sweep analysis are shown in Figure 5. When comparing this figure and Figure 3, it can be seen that voltage gains of SPMIC and MPMIC are equal in CCM. On the other hand, unlike SPMIC, MPMIC is capable to boost the input voltage in DCM when $d_i < d_0'$. Moreover, critical K values are much higher for MPMIC since multiphase structure decreases the inductor current peaks. This observation shows that larger inductors are needed in MPMIC for CCM operation when compared to SPMIC.

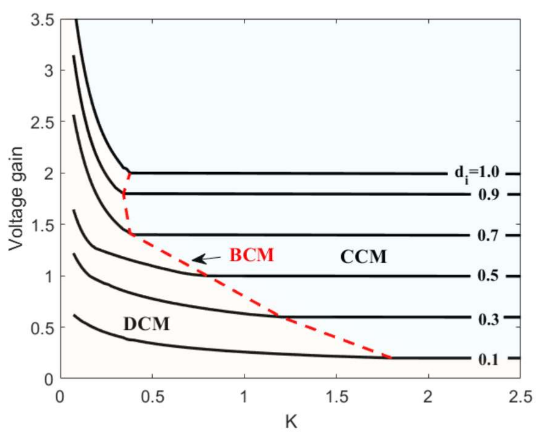

(a)

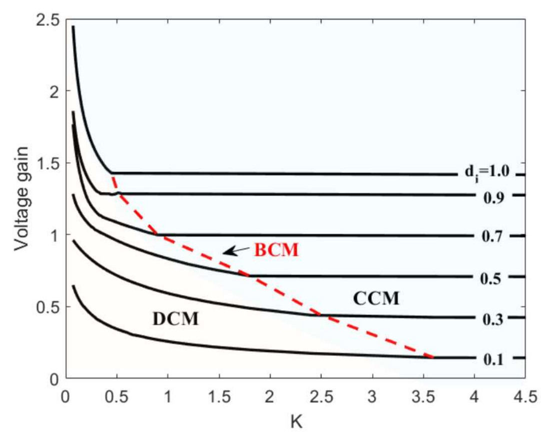

(b)

Figure 5. Discharging mode characteristic curves of MPMIC for CCM, DCM, and BCM regions for(a) $d_0' = 0.5$ and (b) $d_0' = 0.7$.

3.2. Charging mode

Like in SPMIC, similar equations and results for this mode can be obtained similarly by changing the subscripts of duty cycles in the discharging mode.

4. Design considerations

In order to compare SPMIC and MPMIC fairly, they need to be designed by considering same conditions. In this work, the maximum average input current is selected as $7A$, which is dictated by the dc power supplies in our laboratory. Moreover, it is decided that the output voltage is $200V$, and the input voltage range is $175-225V$. In SPMIC, the switching frequency is $48kHz$. Moreover, in MPMIC, the output switches switching frequency is also $48kHz$, while the input switches switching frequency is $16kHz$ for having same effective frequency. Furthermore, the range for d_0 is set to $0.3-0.5$. In the design procedure, V_1 is set to $225V$, while V_2 is set to $175V$.

4.1. Inductors

First of all, the inductor inductances should be determined. Under the assumption that SPMIC operates in CCM, the required inductances for a given inductor current ripple can be calculated based on (7) and (9). From (7), for $d_0' = 0.5$, the duty cycles of the gate signals of S_1 and S_2 can be calculated as 0.44 and 0.57, respectively. Therefore, the maximum inductor currents become $15.9A$ and $12.28A$ for L_1 and L_2, respectively. If the current ripple is set to 10% of 15.9, $1.59A$, the required inductance for L_1 and L_2 can be calculated as approximately $175\mu H$ from (9); furthermore, it is calculated as approximately $250\mu H$ for $d_0' = 0.7$. Therefore, the inductance of SPMIC inductors are selected as $250\mu H$. For a fair comparison, the inductances of MPMIC inductors are also selected as $250\mu H$. In order to check whether the converters operate in CCM or DCM, K and K_{crit} values can be compared. In Table 3, these values are computed for different scenarios. Please note that K_{crit} values for MPMIC are obtained through the interpolation of the characteristic curves given in Fig. 5. According to Table 3, SPMIC is expected to operate in CCM in almost all power regions ($K > K_{crit}$) while MPMIC in DCM.

The peak inductor currents for SPMIC can be computed as $16.64A$ and $12.79A$ for L_1 and L_2, respectively, by letting $d_0' = 0.5$ in (8). Moreover, based on Table 2 and (16), the peak current of L_1 is computed as $11.02A$, while one of the L_2 is computed as $7.66A$ from (16) for MPMIC. Finally, the inductors can be designed. In this work, X-Flux toroids from Magnetic Inc. are preferred. First of all, LI^2 quantities are computed from the determined inductance value ($250\mu H$) and inductor peak currents ($16.64A$ and $11.02A$) as $69.22mH \cdot A^2$ and $30.36mH \cdot A^2$ for SPMIC and MPMIC, respectively. Then, based on the selector chart provided by the manufacturer, 78110 core is selected for SPMIC while 78443 core for MPMIC. By assuming 20% roll-off, the number of turns according to inductance factors of the selected cores are calculated as 63 and 42 for 78110 and 78443 toroids, respectively. In order to limit the skin effect, Litz wires (2x162xAWG#38 for SPMIC and 162xAWG#38 for MPMIC) are utilized to manufacture the inductors. The winding resistances of resultant inductors are measured as $32.3mH$ and $45.9mH$ for SPMIC and MPMIC, respectively.

Table 3. Evaluation of K values for SPMIC and MPMIC.

d_0'	V_i	K @ full power	K @ %10 of full power	K_{crit} for SPMIC	K_{crit} for MPMIC
0.5	175V	0.73	0.073	0.03	0.61
	225V	0.94	0.094	0.03	0.95
0.7	175V	0.73	0.703	0.061	0.71
	225V	0.94	0.094	0.056	1.24

4.2. Semiconductors

For selecting the power switches, the voltage and current stresses on them must be known. The input switches in SPMIC and MPMIC are exposed to the input voltage (maximum $225V$) while the output switches are exposed to the output voltage ($200V$). Moreover, the peak currents of input switches are equal to peak currents of inductors ($16.64A$ and $11.02A$) while the peak current of the output switches are about to the twice of the maximum load current ($28A$) considering the maximum value of d_0, 0.5. Since the converters are hard-switched, a safety margin should be determined for reliable operation considering parasitic effects. Therefore, the MOSFETs given in Table 4 are chosen.

Table 4. Specifications of the prototypes

	SPMIC	MPMIC
Max. Input Current	7A	
Output Voltage	200V	
Input Voltage Range	175-225V	
d_0 range	0.3-0.5	
Output Capacitor	2 parallel 600V 150μF aluminium electrolytic	
Switching Frequency	48kHz	16kHz and 48kHz
Inductance	250uH	
Inductors Peak Current	16.64A	11.02A
Magnetic Cores	78110	78443
Number of Turns	63	42
Winding Resistances	32.3mH	45.9mH
Total Inductor Weight	545g	1187g
Number of MOSFETs	12	16
Input MOSFETs	IXFH20N85X (850V, 20A)	
Output MOSFETs	IXFH30N85X (850V, 30A)	
Gate Drivers	Skyper Pro 32R	

4.3. Output capacitor

For both converters, the required capacitance of the output capacitor for a given voltage ripple can be calculated similarly to how it is calculated in a classical boost converter. For $1V$ voltage ripple, the minimum capacitance can be computed as in

$$C_{0-min} = \frac{I_{o-max} d'_{0-max}}{f \Delta V_o} = \frac{15 \times 0.7}{48k \times 1} = 218 \mu H \tag{17}$$

where I_{o-max} is the maximum load current and ΔV_o is the output voltage ripple. As a result, two parallel connected $600V - 150\mu F$ aluminium electrolytic capacitors are preferred for the output capacitors as given in Table 4. In addition, same PCBs are used for creating the power boards of both converters in a way of connecting the manufactured inductors appropriately. $15A$ Skyper Pro 32R drivers are used for driving MOSFETs. Moreover, a LV25P voltage transducer and a LA55P current transducer are utilized to build the measurement board. PWM signals are created by a TMS320F28335 micro-controller based on the data retrieved from the measurement boards. The control of the converters are realized by two PI controllers with the aim of setting input power levels to share the output power equally among sources as in [27].

5. EXPERIMENTAL STUDY

The specifications of the prototypes built based on the design procedure are summarized in Table 4. Moreover, the photos of the whole system and inductors are given in Figure 6. In this work, SPMIC and MPMIC are constructed by connecting the manufactured inductors to the same power board for practicality. Since the discharging mode and charging mode are similar, the converters are tested only for the discharging mode. Experimental waveforms are given in Figure 7. In Figure 7a, voltage and current waveforms for inductors of SPMIC when output power is $1000W$ and d_0' is 0.6. From this figure, similar waveforms to ones given in Figure 2 can be seen; these waveforms clearly indicate CCM operation and power sharing between sources. Figure 7b shows the inductor voltage and current variations for MPMIC when the output power is $2000W$ and d_0' is 0.7. Similarly, the power sharing between sources is also achieved in MPMIC. It can be observed that these experimental results validates the theoretical waveforms; moreover, L_{1A} operates in DCM, while L_{2A} operates in the vicinity of BCM. Figure 7c shows the output voltage and inductor currents for MPMIC when the first input $(V_1 = 225V)$ power is $1500W$ and d_0' is 0.5. First of all, the output voltage seems to be well-regulated at $200V$ as targeted. Furthermore, the obtained current waveforms correspond to ones plotted in Figure 4. Similarly, In Figure 7d, the output voltage and inductor currents for MPMIC are given when the second input $(V_2 = 175V)$ power is $1300W$, and d_0' is 0.5. From this figure, one can again notice the successful output voltage regulation and alignment between the experimental and theoretical waveforms.

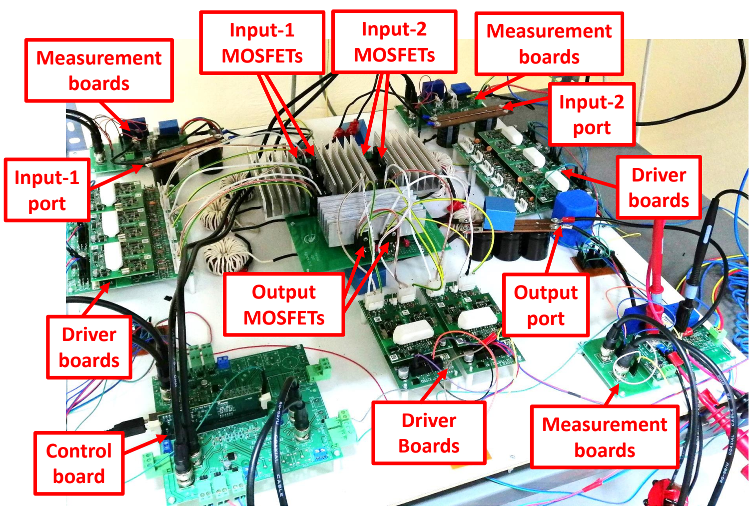

(a)

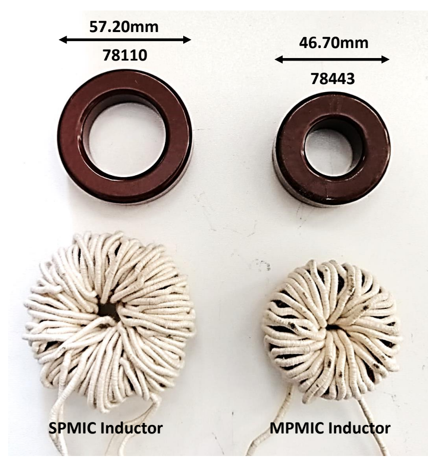

(b)

Figure 6. Photos of the a) prototype, b) inductors.

6. THE COMPARATIVE STUDY

6.1. Voltage-gain

In order to compare the converter prototypes in terms voltage-gain, their nonideal models, including drain-source resistances of selected MOSFETs, winding resistances of manufactured inductors, and forward voltage

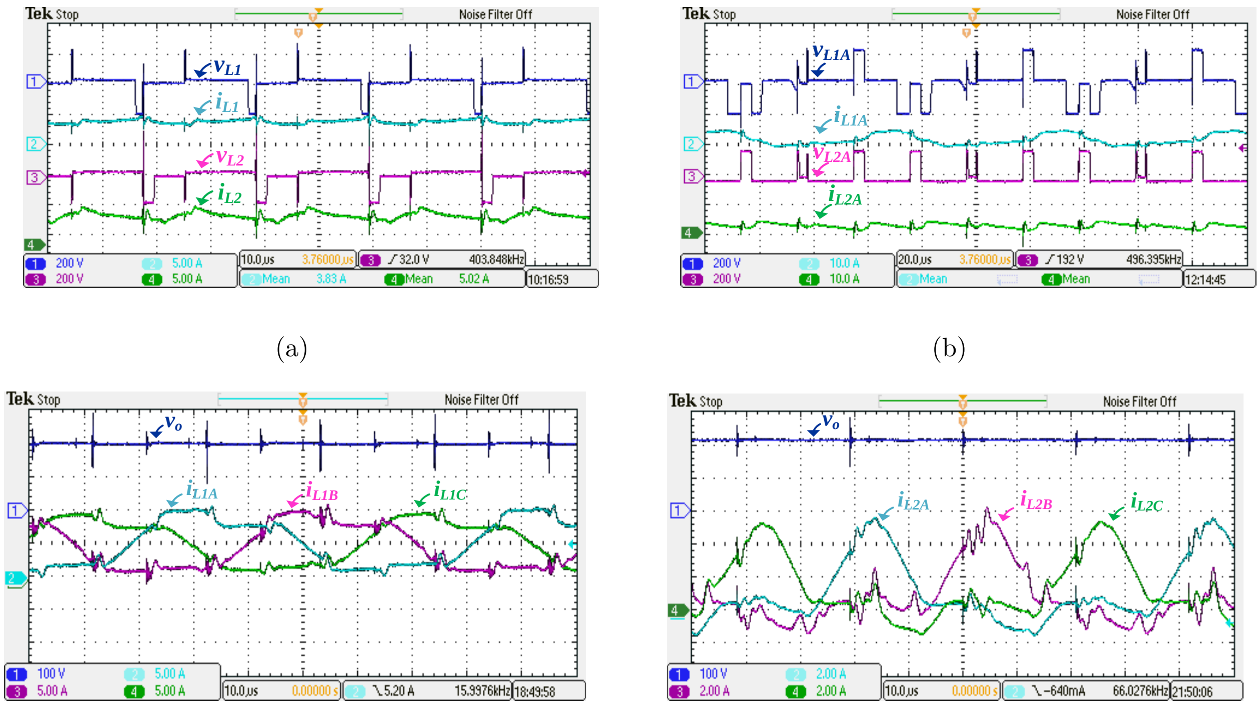

(c) (d)

Figure 7. Experimental result for a) SPMIC when $P_o = 1000W$ and $d_0' = 0.6$, b) MPMIC when $P_o = 2000W$ and $d_0' = 0.7$, c) MPMIC when $P_1 = 1500W$ and $d_0' = 0.5$, d) MPMIC when $P_2 = 1300W$ and $d_0' = 0.5$.

drops of MOSFET body diodes, are created in PSIM. By this way, it is aimed to have realistic results. Through a parametric sweep study based on the created PSIM nonideal models, the results shown in Figure 8a are obtained. According to this figure, MPMIC allows to have more voltage-gain than SPMIC in low-power region. However, the voltage-gains of the converters become equal in high power region, since MPMIC starts to operate in CCM like SPMIC.

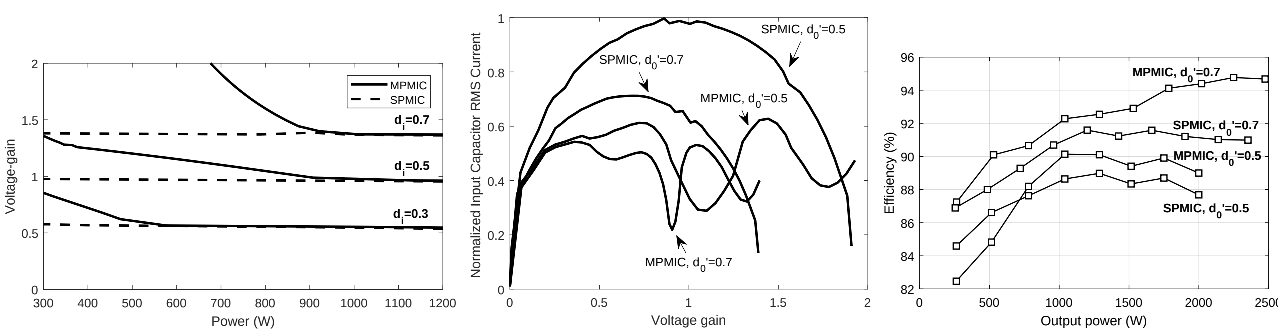

(a) (b) (c)

Figure 8. Comparison of SPMIC and MPMIC in terms of a)voltage-gain, b) input rms current, c) efficiency.

6.2. Input current ripple

Input capacitor root-mean-square (rms) currents of SPMIC and MPMIC are obtained another parametric sweep study based on the non-ideal PSIM models; then, they are normalized by the output current. The results are summarized in Figure 8b. According to this figure, it is clear that MPMIC is superior to SPMIC in terms of input current ripple. Moreover, selecting higher d'_0 decreases input current ripple in both converters thanks to decreased inductor peak currents.

6.3. Efficiency

The efficiency curves of SPMIC and MPMIC are plotted based on the experimental data as in Figure 8c . According to this figure, MPMIC clearly allows to reach more efficient power conversion than SPMIC. There are 2 dominant reasons behind of this improvement: 1) decreased copper losses thanks to decreased rms inductor currents, 2) decreased switching losses thanks to decreased switching frequency and zero-current-switching in DCM. Moreover, higher d'_0 increases the efficiency by decreasing current peaks as observed in [27]. Furthermore, the multiphase structure fails to increase the efficiency in low power region because of the complexity.

6.4. Complexity and cost

The created prototypes of SPMIC and MPMIC reveal that MPMIC results in a slightly more complex structure as expected. Moreover, considering the increased number of inductors, switches, and drivers, MPMIC increases the cost when compared to SPMIC as elaborated in Table 5. However, this extra cost may not be bothersome for a real word application when taking into account the electrical energy saving potential thanks to the improved efficiency.

Table 5. Cost comparison of the prototypes.

	SPMIC	MPMIC
Input MOSFETs	$8 \times \$8.77 = \$70.16$	$12 \times \$8.77 = \$105.24$
Output MOSFETs	$4 \times \$11.38 = \$45.52$	
Magnetic cores	$2 \times \$4.36 = \$8.72$	$6 \times \$3.57 = \$21.42$
Litz wires	$2 \times 4.5m \times \$3.55 = \$31.95$	$6 \times 3.2m \times \$1.77 = \$33.98$
PCB and components	\$73.7	
Output and input filters	$4 \times \$5.93 = \$23.72$	
Total cost	\$253.77	\$303.58

6.5. Power density

In order to compare the power boards of the converters in terms of gravimetric power density, inductor and heat-sink masses are taken into consideration while semiconductor masses are ignored since IXFH20N85X is quite lightweight (6g). Two inductors in SPMIC weigh about $545g$, while six inductors in MPMIC weigh about $1187g$. On the other hand, since SPMIC is less efficient than MPMIC, it needs comparatively bulkier heat-sink. Therefore, the resultant extra mass of SPMIC heat-sink can be roughly calculated as in

$$m = \frac{QR_v}{\Delta T}\rho \tag{18}$$

where Q is the power to be dissipated, R_v is volumetric thermal resistance, ΔT is the allowed temperature rise, and ρ is the density of the material. According to Figure 8c, SPMIC consumes about $100W$ more power than MPMIC under full load. R_v is selected as $80cm^3\ ^oC/W$ by considering $5m/s$ air-flow according to [28] and ΔT is assumed to be 50^oC. Finally, for a aluminium heat-sink ($\rho = 2.79g/cm^3$), the extra mass is calculated as $446.4g$. If R_v is selected as $160cm^3\ ^oC/W$ for $2.5m/s$ air-flow, the extra mass becomes $892.8g$. Therefore, it can be asserted that SPMIC can reach slightly higher gravimetric power density than MPMIC when its heat-sink is cooled effectively; otherwise, MPMIC becomes more advantageous.

7. Conclusion

This paper examines a bidirectional multiinput converter fitted to hybrid EVs by taking single-phase and multiphase cases into consideration. After analysing the proposed MPMIC behaviour in steady state, a design procedure has been followed to manufacture the inductors and choose semiconductors along with output capacitor. Then, the created prototypes have substantiated the analysis. According to the realized comparative study summarized in Table 6, the multiphase multiinput converter (MPMIC) exceeds the single-phase multiinput converter (SPMIC) by voltage-gain and input current ripple. Moreover, the retrieved experimental efficiency curves have showed that about 2% average efficiency improvement (about %4 at full power) can be achieved thanks to multiphase structure. On the other hand, it has been explored that MPMIC increases the complexity and cost. Finally, it has been showed that SPMIC is advantageous in terms of gravimetric power density in the case of efficient cooling; otherwise, MPMIC comes to forefront thanks to improved efficiency. As a result, the proposed MPMIC can be pronounced as a powerful candidate to build up HPS in EVs.

Table 6. Comparison of SPMIC and MPMIC.

	SPMIC	MPMIC	Condition
Voltage gain	Less Same	More Same	Low power High power
Input current ripple	More	Less	-
Efficiency	Less	More	-
Complexity and cost	Less	More	-
Power Density	More Less	Less More	Strong Cooling Weak Cooling

Acknowledgment

This work is founded by the Scientific and Technological Research Council of Turkey-TUBITAK under grant number 118E003.

References

[1] Lukic SM, Cao J, Bansal RC, Rodriguez F, Emadi A. Energy storage systems for automotive applications. IEEE Transactions on Industrial Electronics 2008; 55 (6): 2258-2267.

[2] Onar OC, Kobayashi J, Khaligh A. A fully directional universal power electronic interface for EV, HEV, and PHEV applications. IEEE Transactions on Power Electronics 2012; 28 (12): 5489-5498.

[3] Guo J, Rodriguez R, Gareau J, Schumacher D, Alizadeh M, et all. A Comprehensive Analysis for High-Power Density, High-Efficiency 60kW Interleaved Boost Converter Design for Electrified Powertrains. IEEE Transactions on Vehicular Technology 2020; 69 (7): 7131-7145.

[4] Slah F, Mansour A, Hajer M, Faouzi B. Analysis, modeling and implementation of an interleaved boost DC-DC converter for fuel cell used in electric vehicle. International Journal of Hydrogen Energy 2017; 42 (48): 28852-28864.

[5] Blanes JM, Gutiérrez R, Garrigós A, Lizán JL, Cuadrado JS. Electric vehicle battery life extension using ultracapacitors and an FPGA controlled interleaved buck-boost converter. IEEE Transactions on Power Electronics 2013; 28 (12): 5940-5948.

[6] Li J, Stratakos A, Schultz A, Sullivan CR. Using coupled inductors to enhance transient performance of multi-phase buck converters. In: 2004 IEEE Applied Power Electronics Conference and Exposition; Anaheim, CA, USA; 2004. pp. 1289-1293.

[7] Zhang J, Lai J, Kim R, Yu W. High-power density design of a soft-switching high-power bidirectional dc–dc converter. IEEE Transactions on Power Electronics 2007; 22 (4): 1145-1153.

[8] Garcia O, Zumel P, De Castro A, Cobos, A. Automotive DC-DC bidirectional converter made with many interleaved buck stages. IEEE Transactions on Power Electronics 2006; 21 (3): 578-586.

[9] Baba D. Benefits of a multiphase buck converter. Texas Instruments Incorporated, 2012.

[10] Wong K, Evans D. Merits of multiphase buck DC/DC converters in small form factor applications. Texas Instruments White Paper, 2005.

[11] Hegazy O, Van MJ, Lataire P. Modeling and control of interleaved multiple-input power converter for fuel cell hybrid electric vehicles. In: International Aegean Conference on Electrical Machines and Power Electronics and Electromotion, Joint Conference; Istanbul, Turkey; 2011. pp. 408-414.

[12] Kumar GK, Arunkumar G. Multiple Input Interleaved Boost Converter for Non-Conventional Energy Applications. In: Innovations in Power and Advanced Computing Technologies (i-PACT); Vellore, India; 2019. pp. 1-5.

[13] Mallikarjuna B, Samuel, P. Analysis, modelling and implementation of multi-phase single-leg DC/DC converter for fuel cell hybrid electric vehicles. International Journal of Modelling and Simulation 2020; 40 (4): 279-290.

[14] Elsied M, Oukaour A, Chaoui H, Gualous H, Hassan R et al. Real-time implementation of four-phase interleaved DC–DC boost converter for electric vehicle power system. Electric Power Systems Research 2016; 141: 210-220.

[15] Ayoubi Y, Elsied M, Oukaour A, Chaoui H, Slamani Y et al. Four-phase interleaved DC/DC boost converter interfaces for super-capacitors in electric vehicle application based on advanced sliding mode control design. Electric Power Systems Research 2016; 134: 186-196.

[16] Wen H, Su B. Hybrid-mode interleaved boost converter design for fuel cell electric vehicles. Energy Conversion and Management 2016; 122: 477-487.

[17] Wang B, Xian L, Manandhar U, Ye J, Zhang X et al. Hybrid energy storage system using bidirectional single-inductor multiple-port converter with model predictive control in DC microgrids. Electric Power Systems Research 2019; 173 (1): 38-47.

[18] Kumaresan J, Govindaraju C. PV-tied three-port DC–DC converter-operated four-wheel-drive hybrid electric vehicle (HEV). Electrical Engineering 2020; 102 (4): 2295-2313.

[19] Danyali S, Hosseini SH, Gharehpetian GB. New extendable single-stage multi-input DC-DC/AC boost converter. IEEE Transactions on Power Electronics 2013; 29 (2): 775-588.

[20] Gorji JG, Abbaszadeh K, Bagheroskouei F. A New Two-input And Multi-output Interleaved DC_DC Boost Converter For Satellites Power System. In: 10th International Power Electronics, Drive Systems and Technologies Conference (PEDSTC); Shiraz, Iran; 2019. pp. 236-241.

[21] Buswig YM, Utomo WM, Haron ZA, Bakar A. Modeling of A New Modified Multi-Input Interleaved Boost DC-DC Converter. In: 3rd International Conference on Computer Engineering and Mathematical Sciences (ICEMS); Langkawi, Malaysia; 2014. pp. 247-252.

[22] Kallukaran C, Unnikrishnan L, Koshy RA. Multi-Input Interleaved DC-DC Converter with Low Current Ripple for Electric Vehicle Application. In: International Conference on Current Trends towards Converging Technologies (ICCTCT); Coimbatore, India; 2018. pp. 1-5.

[23] Chen J, Hou S, Sun T, Deng, F, Chen Z. A new interleaved double-input three-level boost converter. Journal of Power Electronics 2016; 16 (3): 925-935.

[24] Akar F, Tavlasoglu Y, Vural B. An energy management strategy for a concept battery/ultracapacitor electric vehicle with improved battery life. IEEE Transactions on Transportation Electrification 2016; 3 (1): 191-200.

[25] Hintz A, Prasanna UR, Rajashekara K. Novel modular multiple-input bidirectional DC-DC power converter (MIPC) for HEV/FCV application. IEEE Transactions on Industrial Electronics 2014; 62 (5): 3163-3172.

[26] Akar F. A bidirectional multi-phase multi-input DC-DC converter. International Conference on Engineering and Technology (ICET); Antalya, Turkey; 2017. pp. 1-5.

[27] Akar F, Tavlasoglu Y, Ugur E, Vural B, Aksoy I. A bidirectional nonisolated multi-input DC–DC converter for hybrid energy storage systems in electric vehicles. IEEE Transactions on Vehicular Technology 2015; 65 (10): 7944-7955.

[28] Seshasayee N. Understanding thermal dissipation and design of a heatsink. Texas Instruments, 2011.

[29] Bakar A, Utomo M, Taufik T, Ponniran A. Modeling of FPGA-and DSP-based pulse width modulation for Multi-Input interleaved DC/DC Converter. International Review of Electrical Engineering 2019; 14, 79-85.